Iranian Journal of Science & Technology, Transaction B: Engineering, Vol. 34, No. B5, pp 471-485
Printed in The Islamic Republic of Iran, 2010

HEAT TRANSFER AND FLUID FLOW THROUGH A RIBBED PASSAGE IN STAGGERED ARRANGEMENT*

A. SOHANKAR

Dept. of Mechanical Engineering, Yazd University, Yazd, I. R. of Iran
Email: asohankar@yazduni.ac.ir

Abstract– Fluid flow and heat transfer are computed through a rib-roughened duct of square cross-section. The staggered ribs are attached along the two opposite walls of the channel to augment heat transfer. Simulations are performed with an incompressible SIMPLEC finite volume collocated code. Five different versions of k-ω and k-ε turbulence models are employed. The molecular Prandtl number is 0.71 and the Reynolds number based on the bulk velocity and the height of the channel is 100000.

The predicted flow field and heat transfer show a relatively good agreement with the experimental results for different employed turbulence models, although the predicted flow field results are much better than the heat transfer results.

Employing a variable turbulent Prandtl number according to the Kays and Crawford relation shows only a small difference in the estimated turbulent heat transfer fluxes. The influence of constant turbulent Prandtl numbers ranging from 0.5 to 0.92 is also examined and it is found that it has a significant effect on the simulation results of the heat transfer.

Keywords– Rib-roughened channel, staggered ribs, heat transfer augmentation, turbulent Prandtl number

1. INTRODUCTION

In the design of thermal systems and engineering apparatus, the prediction of heat transfer and pressure drop performances is an essential task. In recent years, serious attempts have been made to achieve higher heat transfer rates in devices such as heat exchangers, cooling passage for the gas turbine blades, electronic equipment, etc. Substantial energy savings, more compact and less expensive apparatus with higher thermal efficiency are the main reasons for this demand. Vortex generation is a promising technique for heat transfer augmentation. In this method, transversal and longitudinal vortices are passively generated using tools with the vortex generators such as fins, ribs and wings. The use of the surface protuberances is a passive heat transfer augmentation method and is based on developing boundary layers or streamwise fluctuations, creating swirl or vortices and flow destabilization or turbulence intensification [1-3].

An early numerical/experimental investigation regarding the rib-roughened passage for internal cooling was made by Liou et al. [4]. Their results were used to evaluate codes and turbulence models in the 7th ERCOFTAC Workshop. Iacovides [5] performed the computation of the periodic flow and heat transfer through stationary and rotating ducts of a square cross-section, with the rib-roughened walls. The square-sectioned ribs, normal to the flow direction are employed in inline and staggered arrangements. Mean flow predictions were satisfactory while the coefficients of the wall heat transfer were not as close to data as the flow predictions. The effect of thermal boundary conditions on numerical heat transfer

*Received by the editors February 4, 2009; Accepted August 18, 2010.

predictions in a rib-roughened passage is studied by Iaccarino et al.[6]. They reported that some of the discrepancies between the experimental and numerical results can be eliminated when conduction in the rib is taken into account. Bredberg [7] has performed a series of numerical investigations to predict heat transfer and flow field in the ribbed channel, similar to those present in the internal cooling with different turbulence models. The local Nusselt number distributions, the flow pattern, and the friction factors in the rib-roughened channel with a different rib and channel configurations, and the aspect ratio were reported by the researchers, e.g. [8-14].

In the present work, the flow field and heat transfer in a stationary rib roughened passage in a staggered arrangement are predicted for Re=100000 and Pr=0.71. The flow within this type of channel is often turbulent due to the presence of the ribs and the high Reynolds number flow. The five versions of the two-equation turbulence models ($k-\varepsilon, k-\omega$) are employed for the simulations. The study of the influence of the turbulent Prandtl number on the results is also the aim of this work. This paper is organized as follows. In Sec. 2 the flow configuration, computational domain, grid and the boundary conditions are briefly introduced. A short review on the governing equations and turbulence modelling formulation are given in Sec. 3. The analysis of the time-averaged heat transfer and fluid flow results is presented in Sec. 4. Finally, some conclusions are summed up in Sec. 5.

2. FLOW GEOMETRY DESCRIPTION

As illustrated schematically in Fig. 1, the physical problem under consideration is a ribbed passage in a staggered arrangement (e.g. a part of a cooling passage for gas turbine blades). As seen, staggered square ribs are attached along two opposite walls of the channel.

The computational domain and grid for the ribbed channel are shown in Fig. 1. As seen, the flow is described in a coordinate system (*x, y*) in which the *x*-axis is aligned with the inflow, streamwise direction, and the y-axis is perpendicular to the *x*.

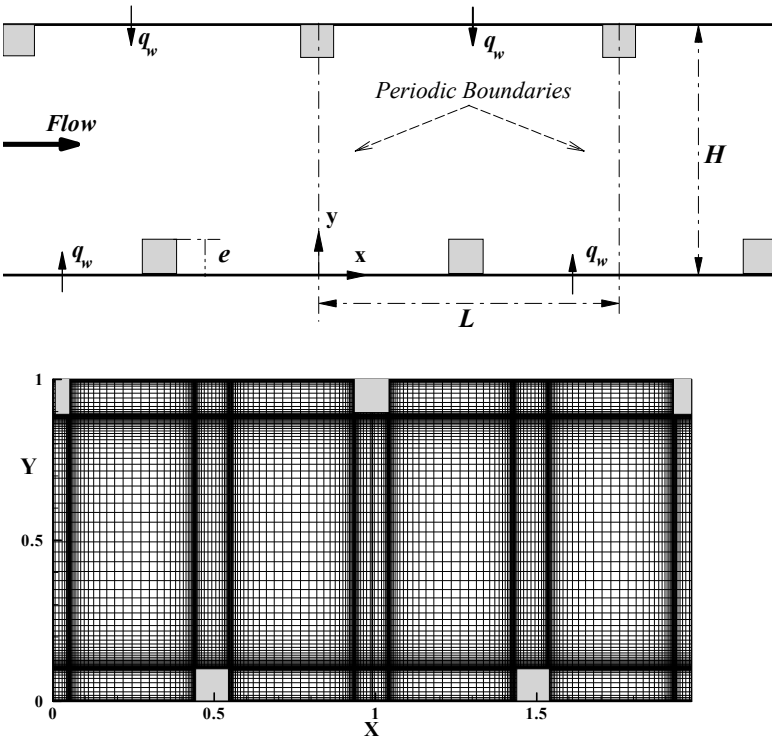

Fig. 1. Grid and geometry of the rib-roughened channel in the staggered arrangement, the computational domain is located between the periodic boundaries

All geometrical lengths are scaled with *H*, the channel height. Velocities are scaled with U_B, bulk velocity. The side of the squared cross-section rib is denoted as *e* and rib-to-rib spacing is referred to as *L*, pitch or distance between two successive ribs. The ratio of the rib-height to the channel-height is called the blockage ratio, e/H, which is chosen as 10%. Pitch to rib height ratio, L/e, is an important parameter, and it is selected as 10 units in the present study. The Reynolds number is defined as $\mathrm{Re} = U_B H / \upsilon$. The local Nusselt number is calculated at the wall as: $Nu(x) = \frac{h(x)H}{k_f}$, $h(x) = -k_f \frac{\partial \theta}{\partial y}|_w / (\theta_w - \theta_B)$, where $h(x)$ θ_w, θ_B and k_f are the local convection heat transfer coefficient, wall and bulk temperatures and conduction coefficient, respectively.

a) Boundary conditions

The problem under consideration repeats itself after a certain distance (pitch) in the streamwise direction (Fig. 1). Thus, the flow will repeat itself in a periodic manner. Consequently, all the quantities except pressure and temperature exhibit a periodic behaviour. In a periodic flow regime, the pressure and temperature are decomposed into a fluctuating term and a linearly varying term in the streamwise direction [15]. Thus, the pressure and temperature may be formulated as $p(x,y) = -\gamma x + \tilde{p}(x,y)$ and $\theta(x,y) = \lambda x + \tilde{\theta}(x,y)$. The terms of $\tilde{p}$ and $\tilde{\theta}$ are fluctuating pressure and temperature, respectively, where they identically repeat themselves in each interval. The factor of γ is the streamwise pressure drop within the rib-interval and it should be calculated iteratively during the simulation based on the selected Reynolds number (or mass flow). For a constant heat flux wall boundary condition, $\lambda = q / \dot{m} c_p L$. The governing equations need to be modified by adding additional source terms, $\gamma \delta_{i1}$ in the momentum equation and $-\rho u_i \lambda \delta_{i1}$ in the energy equation. In summary, the boundary conditions at the inlet and outlet, which are periodic boundaries, are $\phi(ni, j) = \phi(2, j)$ and $\phi(1, j) = \phi(ni - 1, j)$, where ϕ denotes the velocity component, the fluctuating pressure, $\tilde{p}$, the fluctuating temperature, $\tilde{\theta}$, and turbulent properties, k, ε, ω. No slip boundary condition is employed on the walls and ribs. A constant heat flux was set on the walls, (Fig. 1).

3. GOVERNING EQUATIONS & TURBULENCE MODELS

Applying the Reynolds decomposition to the incompressible and the constant property instantaneous momentum and energy equations, and taking the average of all terms, the time averaged equations are obtained as:

$$u_{i,i} = 0 \tag{1}$$

$$(\rho u_i u_j)_{,j} + p_{,i} = \mu u_{i,jj} + \tau_{ij,j} \tag{2}$$

$$c_P \rho (\theta u_j)_{,j} = k_f \theta_{,jj} + q_{j,j} \tag{3}$$

Here, $\tau_{ij} = -\rho \overline{u_i' u_j'}$ and $q_j = -c_P \rho \overline{u_j' \theta'}$ are referred to as the Reynolds stress tensor and turbulent heat fluxes, respectively. Based on the Boussinesq's assumption, the Reynolds stress is equal to a scalar, which is called the eddy viscosity, times velocity gradient and it may be written as $\tau_{ij} / \rho = -\overline{u_i' u_j'} = \nu_t (u_{i,j} + u_{j,i}) - \frac{2}{3} k \delta_{ij}$, where $k = \overline{u_i' u_i'} / 2$ is the turbulent kinetic energy and ν_t is the turbulent eddy viscosity. Eddy viscosity, ν_t, is not a fluid property but depends on the state of turbulence and varies significantly from flow to flow. In a direct analogy to the turbulent momentum transport, the turbulent heat is often assumed to be related to the temperature gradient and may be expressed as

$q_j / \rho = -\overline{u_j'\theta'} = \Gamma_t \theta_{,j}$, where Γ_t is the turbulent diffusivity of the heat and it is also not a fluid property but depends on the state of the turbulence. The eddy diffusivity is usually related to the turbulent eddy viscosity and is defined as $\Gamma_t = \nu_t / \mathrm{Pr}_t$, where Pr_t is the turbulent Prandtl number.

The most popular models for a wide range of engineering analysis and research are two-equation turbulence models. These models provide independent transport equations for both the turbulence length and the velocity scales or some equivalent parameters. Of various turbulence models, the two-equation eddy viscosity models, especially $k-\varepsilon$ and $k-\omega$, are frequently used. A brief review on different versions of turbulence models which are employed in this work is given in the following.

The $k-\omega$ model is a popular two-equation model. In this model, the standard k equation is used, but an equation for the new variable, ω, is employed for determining the length scale, $\ell \sim k^{0.5}/\omega$. The ω is often called specific dissipation or the rate of dissipation of energy in unit volume and time and has the dimension s^{-1}, i.e. inverse to time. The high Reynolds number $k-\omega$ model of Wilcox [16] is:

$$\rho \partial_t k + \rho (u_j k)_{,j} = \tau_{ij} u_{i,j} - \beta^* \rho k \omega + ((\mu + \frac{\mu_t}{\sigma_k}) k_{,i})_{,i} \tag{4}$$

$$\rho \partial_t \omega + \rho (u_j \omega)_{,j} = \alpha \frac{\omega}{k} \tau_{ij} u_{i,j} - \beta \rho \omega^2 + ((\mu + \frac{\mu_t}{\sigma_\omega}) \omega_{,i})_{,i} + \chi \tag{5}$$

Where eddy viscosity and the closure coefficients are:

$$\mu_t = \rho k / \omega,\ \alpha = 5/9, \beta = 3/40,\ \beta^* = 0.09,\ \sigma_k = 2,\ \sigma_\omega = 2,\ \chi = 0 \tag{6}$$

The Abid et al. $k-\omega$ model [17] is similar to the above model. The main difference between these models is the definition of the specific dissipation, where it is defined as dissipation divided by kinetic energy in the Abid et al. model, $\omega = \varepsilon / k$, while a closure coefficient is included in the definition by the Wilcox model [16], $\omega = \varepsilon / (\beta^* k)$. The eddy viscosity and the closure coefficients in this model are:

$$\mu_t = C_\mu \rho k / \omega,\ \alpha = 0.55, \beta = 0.83,\ \beta^* = 1, \sigma_k = 1.4,\ \sigma_\omega = 2,\ C_\mu = 0.09,\ \chi = 0 \tag{7}$$

Most of the turbulence models such as the aforementioned methods assume that all regions, even those very close to the wall, are fully turbulent. These types of models are often referred to as the high Reynolds number models, *HRNM*. One can modify the *HRNM* to use them correctly in all parts of the flow. These modified models are called low-Reynolds number turbulence models, *LRNM*.

The Wilcox *LRNM* $k-\omega$ [18] is obtained, if one employs the damping functions, eddy viscosity and the closure coefficients in Eqs. (4) and (5) as:

$$\mu_t = \alpha^* \rho k / \omega, \alpha^* = \frac{\alpha_0^* + \mathrm{Re}_t / R_k}{1 + \mathrm{Re}_t / R_k}, \beta^* = 0.09 \frac{5/18 + (\mathrm{Re}_t / R_\beta)^4}{1 + (\mathrm{Re}_t / R_\beta)^4}, \alpha = \frac{5(\alpha_0^* + \mathrm{Re}_t / R_\omega)}{9\alpha^* (1 + \mathrm{Re}_t / R_\omega)} \tag{8}$$

$$\alpha_0 = 0.1, \beta = 3/40, \alpha_0^* = \beta / 3, \sigma_k = 2, \sigma_\omega = 2, R_k = 2.7, R_\omega = 6, R_\beta = 8,\ \chi = 0 \tag{9}$$

Where the turbulent Reynolds number is defined as $\mathrm{Re}_t = k/(\omega\nu)$ and the turbulent production is $P_k = 2\nu_t s_{ij} u_{i,j}$.

The $k-\omega$ Peng et al. model [19] is similar to the Wilcox *LRNM* $k-\omega$, however, with a cross-diffusion term (χ) added in the ω equation. In this model, the damping functions, eddy viscosity and the closure coefficients in Eqs. (4) and (5) are:

$$\chi = C_\omega \frac{\nu_t}{k} k_{,j}\omega_{,j},\ \beta^* = C_k f_k,\quad \alpha = C_{\omega 1} f_\omega \tag{10}$$

$$\mu_t = C_\mu f_\omega \rho k/\omega,\ f_k = 1 - 0.722\exp(-(R_t/10)^4),\ f_\omega = 1 + 4.3\exp(-(R_t/1.5)^{0.5}) \tag{11}$$

$$f_\mu = 0.025 + [1 - \exp(-(R_t/10)^{0.75}][0.975 + \frac{0.001}{R_t}\exp(-(R_t/200)^2)] \tag{12}$$

$$C_\mu = 1.0,\ C_k = 0.09, C_\omega = 0.75,\ C_{\omega 1} = 0.42,\ C_{\omega 2} = 0.075,\ \sigma_k = 0.8,\ \sigma_\omega = 1.35 \tag{13}$$

Abid et al. low Reynolds number $k-\varepsilon$ model [17] is also employed in the present study.

$$\rho\partial_t k + \rho(u_j k)_{,j} = \tau_{ij}u_{i,j} - \rho\varepsilon + ((\mu + \frac{\mu_t}{\sigma_k})k_{,i})_{,i} \tag{14}$$

$$\rho\partial_t \varepsilon + \rho(u_j \varepsilon)_{,j} = C_{\varepsilon 1}\frac{\varepsilon}{k}\tau_{ij}u_{i,j} - C_{\varepsilon 2} f\rho\frac{\varepsilon^2}{k} + ((\mu + \frac{\mu_t}{\sigma_\varepsilon})\varepsilon_{,i})_{,i} \tag{15}$$

Where eddy viscosity, damping function and the closure coefficients are as:

$$\mu_t = \rho C_\mu k^2/\varepsilon,\ C_{\varepsilon 1} = 1.39,\ C_{\varepsilon 2} = 1.83,\ C_\mu = 0.088,\ \sigma_k = 1.0,\ \sigma_\varepsilon = 1.3 \tag{16}$$

$$f = 1 - \exp(-R_n/12.5),\ R_n = n\sqrt{k}/\nu \tag{17}$$

An incompressible SIMPLEC finite volume collocated code is used in the present study. The solution method for the time averaged governing equations (Eqs. 2-5, 14 and 15) is the finite-volume method and they are written in a general transport equation for a variable Φ:

$$\frac{\partial\rho\Phi}{\partial t} + \frac{\partial}{\partial x_m}(\rho u_m \Phi) = \frac{\partial}{\partial x_m}(\Gamma\frac{\partial\Phi}{\partial x_m}) + S \tag{18}$$

where S denotes the source term per unit volume for the variable Φ (e.g. u_m, θ, k, ε and ω in this study).

The Hybrid differencing scheme is used to approximate the convective fluxes. In this scheme, based on the value of the local Peclet number, a central or upwind differencing approach is employed. The diffusive terms are discretized using central differencing, which is of second order accuracy. The residuals for the continuity, momentum and energy are normalized with the incoming mass flux, momentum flux and energy flux, respectively. The convergence criterion is set to 0.001.

4. RESULTS AND DISCUSSION

a) Flow field results

The normalized streamwise velocity profile is displayed in Fig. 2 for different turbulence models and grids together with the experimental results [20] at the computational inlet (x=0). These plots are provided to show the effect of the grid and turbulence models. As seen, the influence of using a finer grid for the various turbulence models is negligible, especially close to the walls. Although the differences in the central part of the channel are higher where the relatively coarser grids are employed in comparison with the near walls, they are not notable. If one compares the velocity profiles in Fig. 2 for different turbulence models, it is observed that all models predict relatively similar results. The most significant differences

among the models occur around the central part of the channel, especially for the Wilcox models [16, 18]. Of these turbulence models, the Peng et al. model [19], where a cross-diffusion term in the ω equation is added, provides the best agreement with the experimental results.

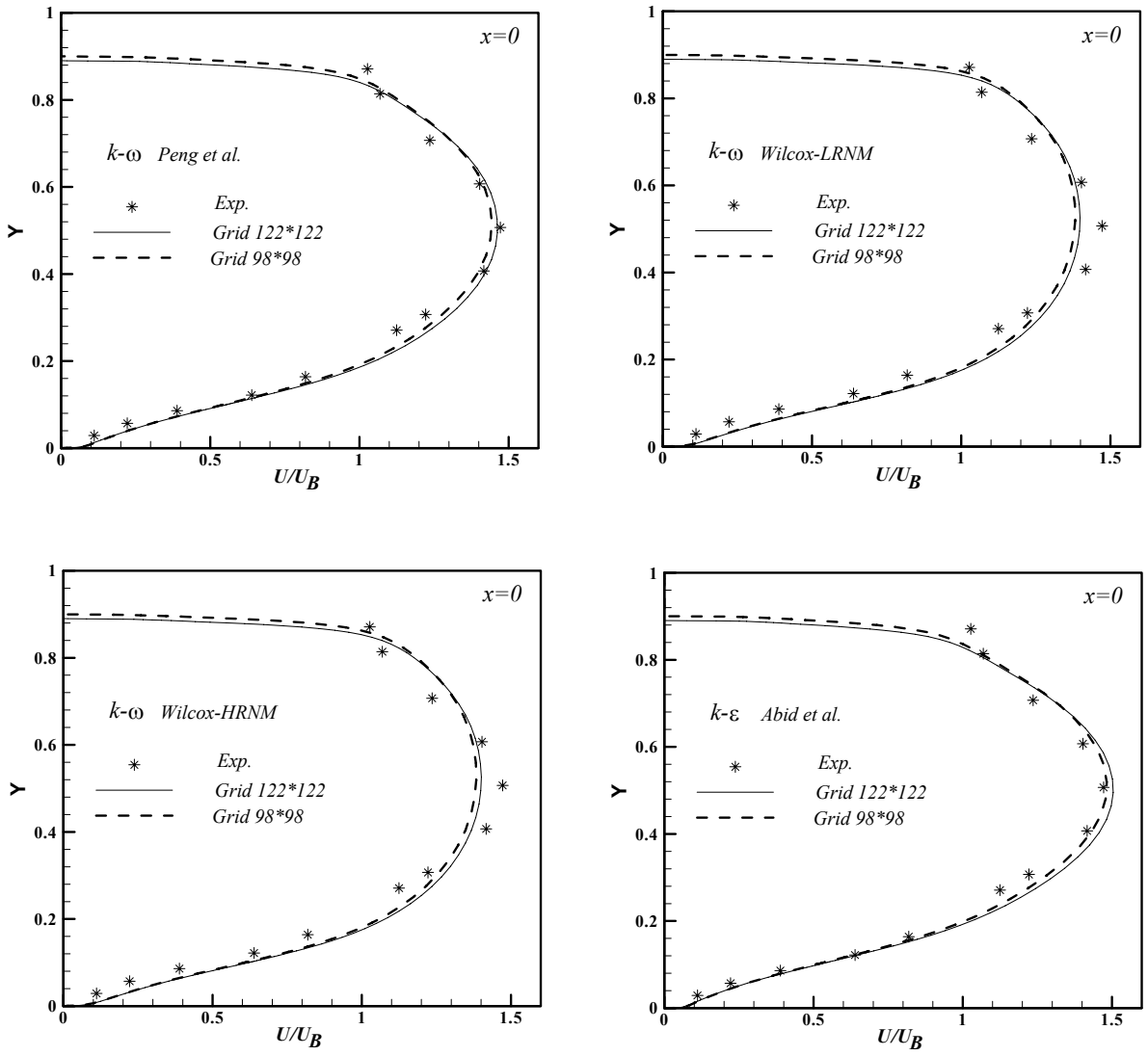

Fig. 2. Normalized streamwise velocity profile at the inlet of the computational domain, x=0, for different turbulence models and grids together with the experimental result [20]

The normalized streamwise velocity profiles are depicted in Fig. 3. These plots are provided for four selected positions in the stream wise direction, i.e. x=0, 0.25, 0.5, 0.75, for different turbulence models, Grid 122×122. As seen, the agreement between the calculated results and experimental ones is qualitatively good for all models. The best agreement exists near the walls, while the differences are higher in the central part of the velocity profiles. It is believed that some part of these differences is due to the use of relatively coarser grids in this region in comparison with those which are employed close to the walls. It is important to mention that the distance between the first grid line and the wall is $\Delta y \approx 10^{-4}$ and this value is corresponds to about $y^+ < 1$, (Fig. 1). As observed from Fig. 3, the turbulence models can improve the results, especially in the central region. The Peng et al. model [19] provides the best agreement in comparison to the other models which are employed in this study. The predicted re-

circulation regions with the negative velocity near the wall are also observed in the profile plots at x=0.25 and x=0.75 (Fig. 3). The maximum absolute velocity (U_{BF}) in the back flow occurs at the 6th node from the wall ($\Delta y \approx 3.5\times10^{-3}$ or $y^+ < 10$) in the case of x=0.75 for the used $k-\omega$ models of the present work. The U_{BF} has a relatively similar value with about 0.24 for these cases, while the predicted value for the $k-\varepsilon$ model occurs at the 7th node from the wall with a lower value, about 0.18.

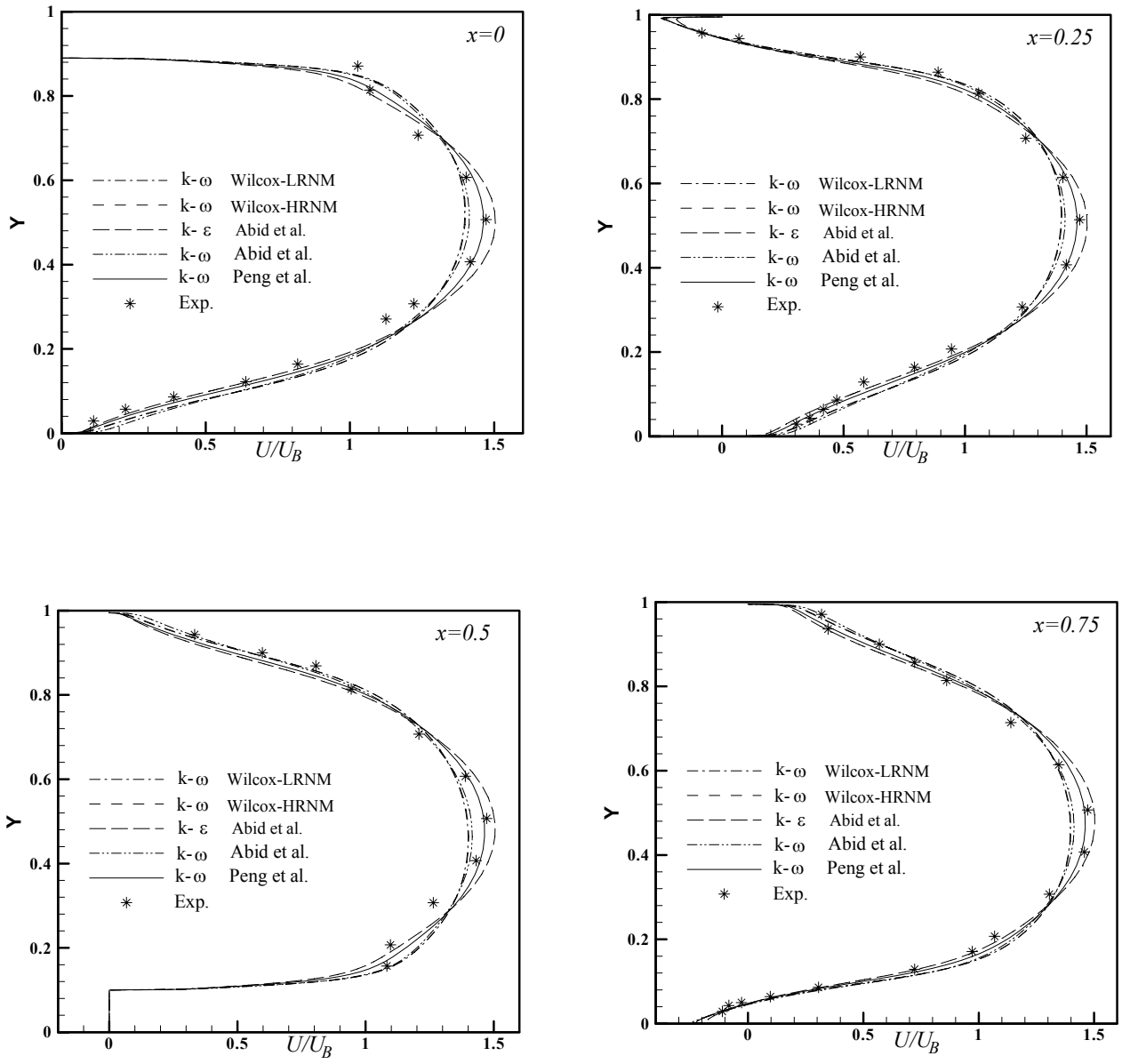

Fig. 3. Normalized streamwise profile at four chosen positions in the streamwise direction (x=0,0.25,0.5,0.75) for different turbulence models, Grid 122×122 Together with the experimental result [20]

The normalized shear stress profiles are plotted for four selected positions in the streamwise direction, i.e. x=0, 0.25, 0.5, 0.75, for different turbulence models, Grid 122×122 in Fig. 4. They are scaled with the squared bulk velocity. The agreement between the predicted and the experimental results close to the walls is good, especially at x=0, 0.25, 0.75. The differences between the results become higher far from

the walls and the top of the ribs. Using relatively coarser grids in this region in comparison with those which are employed close to the walls is a possible reason. As it can be seen in these plots for different turbulence models, the Peng et al. and the $k-\varepsilon$ models totally achieve the best agreement with the experimental data.

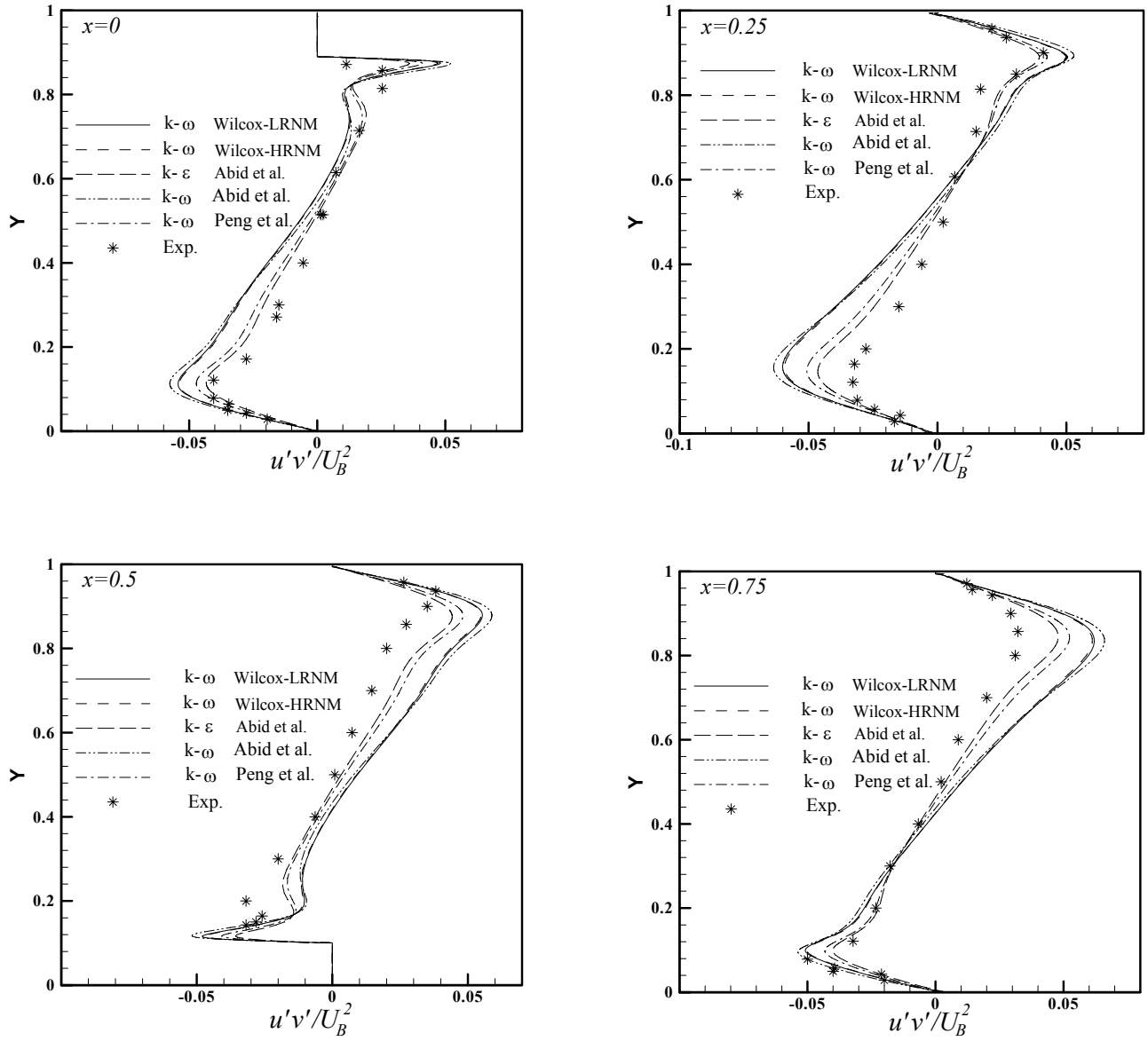

Fig. 4. Normalized shear stress profile at four chosen positions in the stream wise direction (x=0,0.25,0.5,0.75) for different turbulence models, Grid 122×122 together with the experimental result [20]

The streamlines, the contours of the streamwise and normal velocities (u,v), the spanwise vorticity ($\Omega_z = \partial v/\partial x - \partial u/\partial y$), pressure ($p$), temperature, kinetic energy (k) and shear stresses ($u'v'$) are depicted in Fig. 5. As seen from the streamlines plot, the flow separates from the downstream corners of the ribs and is reattached on the walls. Due to the separation of flow, large re-circulation bubbles form, (see also the contours of velocity components and pressure in Fig. 5). The normalized length of these bubbles is about $(3.7-4)e$ for different turbulence models, which are employed in the present study (e is the rib length). It is important to mention that the friction velocity, wall shear stress and y^+ are zero

at the separation and reattachment points. The flow also separates from the upstream corners of the ribs and is reattached on the top of the ribs. The recirculation bubble length on the ribs top depends on the used turbulence models, Fig. 6. This length is measured roughly 40% of the rib length for the employed $k-\omega$ models, while it is about 20% for the $k-\varepsilon$ model. In addition to forming recirculation zones of the downstream and top of the ribs, re-circulation zones are also produced in front of the ribs due to the flow separation from the walls, (Fig. 6). The size of this type of bubble also depends on the employed turbulence models, where it is approximately 70% and 40% of the rib length for the used $k-\omega$ models and $k-\varepsilon$ model, respectively. As seen from the vorticity contours in Fig. 5, there are strong vorticity levels in the re-circulating regions. The levels of the kinetic energy (k) and shear stresses ($u'v'$) are also high in the separation regions, especially in the region around the upstream corners of the ribs, where the flow suddenly accelerates and changes its direction.

The friction coefficient ($f = 2\tau_w / \rho U_B^2$) along the lower ribbed wall and pressure profile at three positions in the streamwise direction are shown in Fig. 7. As seen, all $k-\omega$ models yield relatively similar values, while the $k-\varepsilon$ model predicts a higher friction coefficient. Because there is a strong connection between the flow field (or friction coefficient) and heat transfer (or Nusselt number), such a notable difference will be also observed for the heat transfer results (see next chapter).

b) Heat transfer results

In the present study, constant heat flux is applied on the upper and lower walls, while the ribs are thermally insulated, Fig. 1. It is important to mention that the experimental data [18] are provided for the same geometry as is shown in Fig. 1. In experiments, heaters were attached on the walls and provided a constant heat flux. A zero heat flux was applied on the ribs, where they were isolated from the heaters.

The major difficulty in a numerical calculation of heat transfer is the proper selection of the turbulence model. The turbulent heat is commonly calculated as: $q_j / \rho = -\overline{u_j'\theta'} = \Gamma_t \theta_{,j}$, where Γ_t is the turbulent diffusivity of heat. The Γ_t is not a fluid property, but it depends on the state of the turbulence. The eddy diffusivity is usually related to the turbulent eddy viscosity and it is defined as $\Gamma_t = \nu_t / \mathrm{Pr}_t$, where Pr_t is the turbulent Prandtl number. The turbulent Prandtl number is suggested by "Reynolds analogy" to be constant and equal to unity. This simple assumption ($\mathrm{Pr}_t = 1$) sometimes provides good, although mostly overestimated, computational results for heat transfer. However, turbulent Prandtl number is not generally a constant, and the thermal diffusivity is not necessarily related to the eddy diffusivity. It is reported that the turbulent Prandtl number is a function of molecular Prandtl number. For example, a turbulent Prandtl number model was proposed by Mynog and Kasagi [22] as: $\mathrm{Pr}_t = 0.75 + 1.63/\ln(1 + \mathrm{Pr}/0.0015)$ for $0.01 < \mathrm{Pr} < 50000$ (where $\mathrm{Pr} = 0.71 \Rightarrow \mathrm{Pr}_t \cong 1$). Most researchers commonly adopt a constant turbulent Prandtl number of less than one for air, e.g. $\mathrm{Pr}_t = 0.92$, for flow configuration similar to the present study[5-7]. $\mathrm{Pr}_t = 0.7$ has more commonly been used [20]. Here, the effect of turbulent Prandtl numbers ($\mathrm{Pr}_t = 0.5 - 0.92$) is examined in the present simulations. In this work, we have tried to compare the simulation results for two cases. First, a constant turbulent Prandtl number is employed for the whole computation domain. In the second case, the turbulent Prandtl number is calculated during simulations based on an empirical formula suggested in Ref. 24

The calculated local Nusselt numbers on the lower wall together with the experimental result [21] are plotted for different grids (98×98 and 122×122), turbulent Prandtl numbers ($\mathrm{Pr}_t = 0.5 - 0.92$) and turbulence models ($k-\omega$, $k-\varepsilon$) in Fig. 8. The predicted results of these simulations for two different meshes are compared with the experimental results in Fig. 8. As observed, the finer grid has a notable effect on the Nusselt number, where the Nusselt numbers reach a higher numerical level for the finer grid. Although using finer grids does have a small influence on flow field, (Figs. 2 and 3), this effect is larger for predicting the heat transfer and Nusselt number.

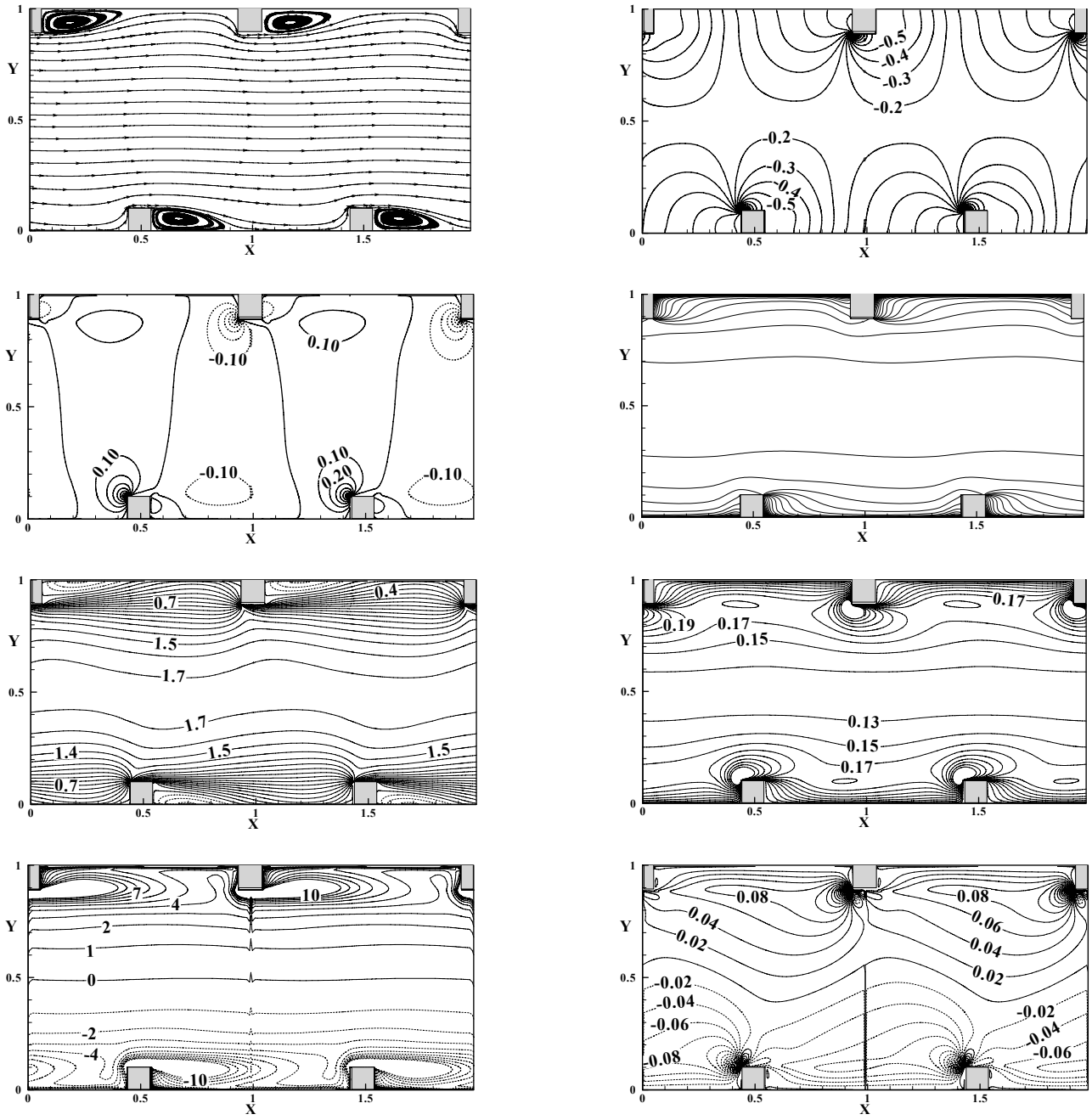

Fig. 5. From top to bottom, Left: streamlines, the contours of the stream wise and normal velocities, and span wise vorticity, Right: the contours of the pressure, temperature, kinetic energy and shear stresses. The solid and dash lines show the negative and positive values, respectively, Grid 122×122, Wilcox HRNM

The effect of the constant turbulent Prandtl numbers, Pr_t, ranging from 0.5 to 0.92, is examined for different turbulence models and grids, Fig. 8. As seen, when Pr_t decreases from 0.92, the numerical level of the Nusselt Number increases. This is clearly observed from the Nusselt profile plot for the Wilcox LNRM [18] model, where the best agreement with the experimental results occurs in the case $\mathrm{Pr}_t = 0.5$. A similar behaviour is observed for the Wilcox HNRM [16], Peng et al. [19] and $k-\varepsilon$ [17] turbulence models in Fig. 8. It is clear that an increase in the Pr_t causes a decrease in the turbulent diffusivity of heat, $\Gamma_t = \nu_t / \mathrm{Pr}_t$, thus a corresponding decrease in the turbulent heat transfer and local Nusselt number occurs.

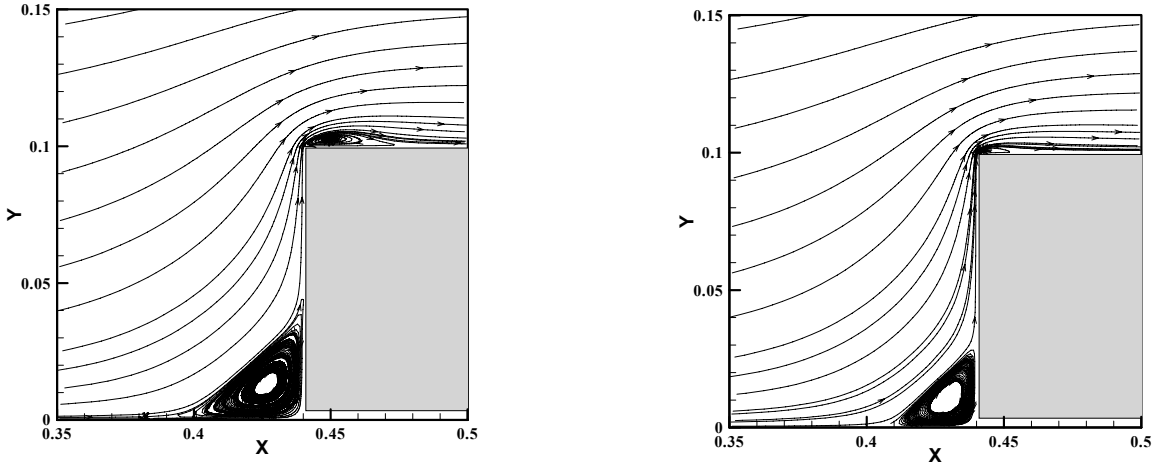

Fig. 6. Details of the streamlines close to the upstream and the top of the rib,
Left: $k-\omega$ model [18], Right: $k-\varepsilon$ model [17]

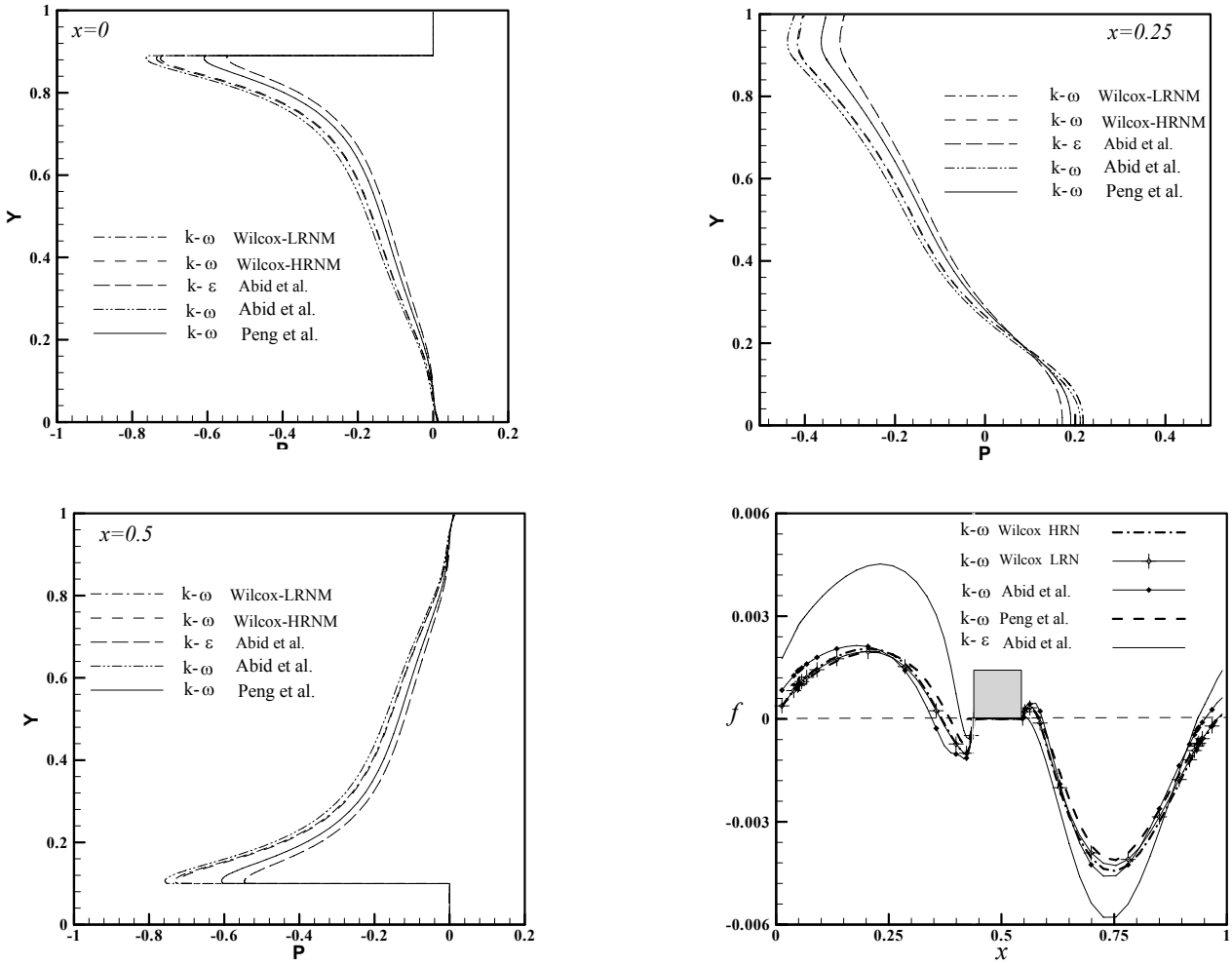

Fig. 7. Pressure profile at the three chosen positions in the streamwise direction (x=0,0.25,0.5) and friction coefficient (f) on the lower wall for different turbulence models, Grid 122×122

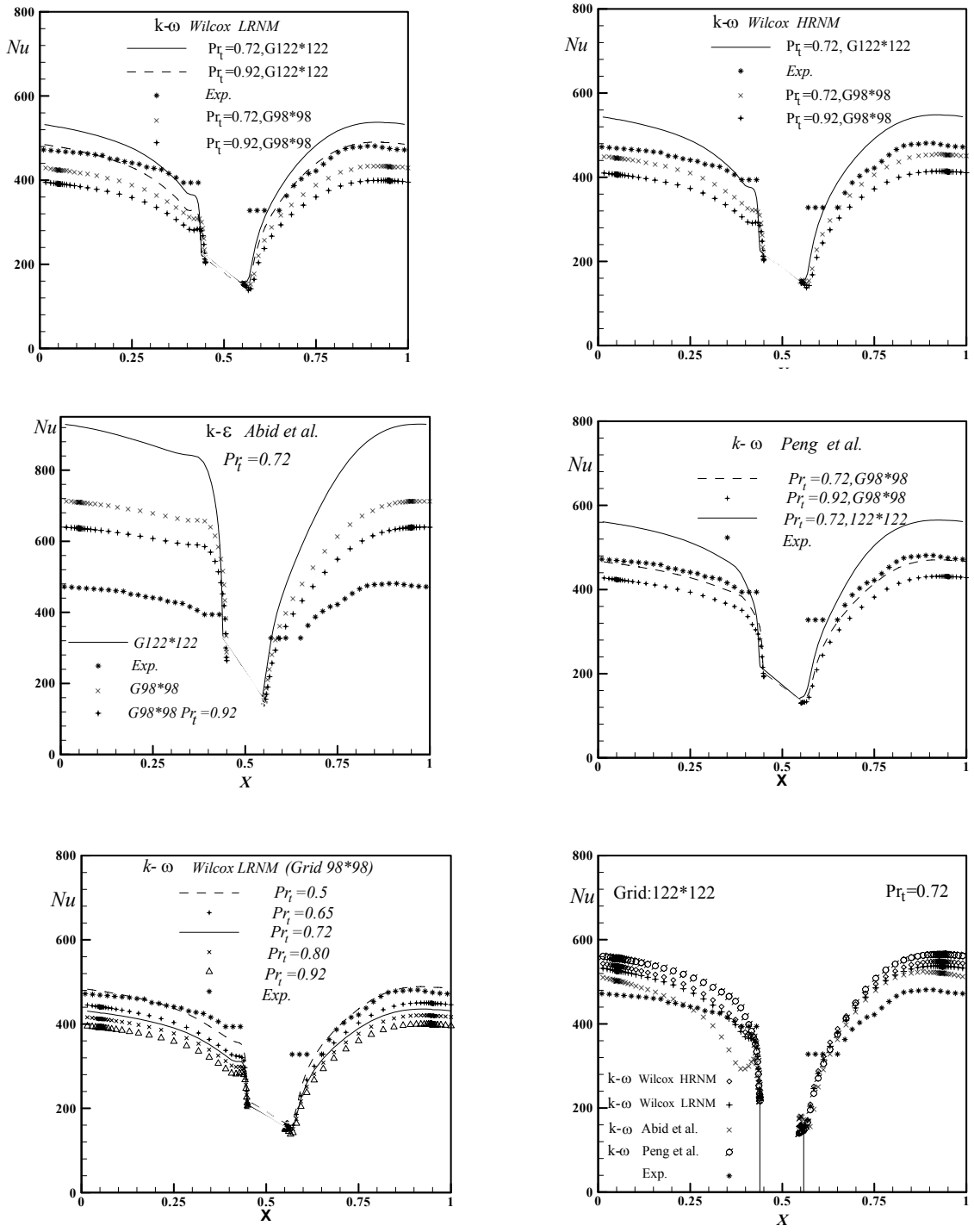

Fig. 8. Local Nusselt number on the lower wall of the channel for different turbulence models, turbulent Prandtl numbers, Pr_t, and grids together with the experimental result [21]

In general, all employed turbulence models except $k-\varepsilon$ predict reasonable agreement with the experimental data when one employs a suitable grid and turbulent Prandtl number, (Fig. 8). For example, the Peng et al. model shows the best agreement with the experimental data for $\mathrm{Pr}_t = 0.72\,(98\times 98)$, while excellent agreement is observed for Wilcox LNRM at $\mathrm{Pr}_t = 0.5\ (98\times 98)$.

As seen in Fig. 8, there is a notable difference between the predicted Nusselt numbers of the $k-\omega$ and $k-\varepsilon$ models. This difference relates to the calculated turbulent viscosity. The present work shows that the $k-\varepsilon$ model generates high and overestimated levels of turbulent viscosity and kinetic energy than the $k-\omega$ models, thus it predicts the highest Nusselt number through the heat transfer model, (Fig. 8).

In the present study, the variable Pr_t according to the Kays and Crawford relation [24] is also applied. Based on Ref. 21, the turbulent Prandtl depends on the turbulent Reynolds number, $\mathrm{Re}_t = \nu_t / \nu$, as: $\mathrm{Pr}_t = 1/\{0.5882 + 0.228(\nu_t/\nu) - 0.0441(\nu_t/\nu)^2[1-\exp(-5.165\nu/\nu_t]\}$.

The use of the above empirical formula suggested in Ref. [24] for the turbulent Prandtl number instead of using a constant value only made a small difference in the estimated value of the Nusselt number.

In general, modelling of the turbulent heat flux is still problematic and the present results show that the way of turbulent heat flux modelling by means of employing a constant or varying turbulent Prandtl number seems to be sufficient in the region without separation. Of course, using a suitable grid and turbulent Prandtl numbers can improve the results in these regions.

5. CONCLUSION

Applicability of five turbulence models to the prediction of fluid flow and heat transfer was examined through a rib-roughened channel. These models are evaluated through comparison with the available experimental results. Some main findings are:

1- The normal and shear stresses, velocity profiles and turbulent quantities predict relatively similar results for different employed turbulence models. Of these turbulence models, the Peng et al. model, where a cross-diffusion term is added in the ω equation, provides the best agreement with the experimental results.

2- A notable difference is found between the predicted Nusselt numbers of the $k-\omega$ and $k-\varepsilon$ models. This is because the $k-\varepsilon$ model generates higher levels of turbulent viscosity and kinetic energy than the $k-\omega$ models, thus it predicts the overestimated Nusselt number through the heat transfer model.

3- The way of turbulent heat flux modelling by means of employing a constant or varying turbulent Prandtl number seems to be sufficient if one employs a suitable grid and turbulent Prandtl number.

4- The turbulent Prandtl number has a significant effect on the calculation results of the heat transfer.

NOMENCLATURE

c_P	specific heat
f	friction coefficient
H	channel height
$h(x)$	local convection heat transfer coefficient
k_f	fluid conduction coefficient
k	turbulent kinetic energy
Nu	Nusselt number
P	static pressure
Pr	molecular Prandtl number
Pr_t	turbulent Prandtl number
Re	Reynolds number
$u_i(u,v)$	velocity components
U	streamwise velocity

U_B bulk velocity
U_{BF} maximum absolute velocity in the back flow
ρ density
θ temperature
ε dissipation rate
ω specific dissipation rate
μ dynamic viscosity
μ_t turbulent viscosity
Ω_z spanwise vorticity

REFERENCES

1. Sohankar, A. (2007). Heat transfer augmentation in a rectangular channel with a vee-shaped vortex generator. *I .J. of Heat and Fluid Flow*, Vol. 28, pp. 306-317.
2. Sohankar, A. (2004). The LES and DNS simulations of heat transfer and fluid flow in a plate-fin heat exchanger with vortex generators. *Iranian Journal of Science & Technology: Transaction B: Technology, Engineering*, Vol. 28, pp. 443-452.
3. Sohankar, A., & Davidson, L. (2001). Effect of Inclined Vortex Generators on Heat Transfer Enhancement in a Three Dimensional Channel. *Numerical Heat Transfer*. Part A. Vol. 39, pp. 433-448.
4. Liou, T. M., Hwang, J. J. & Chen, S. H. (1993). Simulation and measurement of enhanced turbulent heat transfer in a channel with periodic ribs on one principal wall. *I. J. Heat and Mass Transfer*, Vol. 36, pp. 507-517.
5. Iacovides, H. (1998). Computation of flow and heat transfer through rotating ribbed passages. *I. J. of Heat and Fluid Flow*, Vol. 19, pp. 393-400.
6. Iaccarino, G., Ooi, A., Durbin, P. A. & Behnia, M. (2002). Conjugate heat transfer predictions in two-dimensional ribbed passages. *I. J. Heat and Fluid Flow*, Vol. 23, pp. 340-345.
7. Bredberg, J. (2002). Turbulence modelling for internal cooling of gas-turbine blades, Ph.D. thesis. Department of Thermo and Fluid Dynamics, Chalmers University of Technology, Sweden.
8. Liou, T. M., Chen, S. H. & Tsai, T. W. (2000). Heat transfer and fluid flow in a square duct with 12 different shaped vortex generators. *J. of Heat Transfer*, Vol. 122, pp. 327-335.
9. Kiml, R., Mochizuki, S. & Murata, A. (2001). Effects of rib arrangements on heat transfer and flow behaviour in a rectangular rib-roughened passage. *J. of Heat Transfer*, Vol. 123, pp. 675-681.
10. Hsieh, S. S. & Tsai, H. H. & Chan, S. C. (2004). Local heat transfer in rotating square-rib-roughened and smooth channels with jet impingement,. *I. J. Heat and Mass Transfer*, Vol. 47, pp. 2769-2784.
11. Iacovides, H. & Raisee, M. (1999). Recent progress in the computation of flow and heat transfer in internal cooling passages of turbine blades. *I. J. of Heat and Fluid Flow*, Vol. 20, pp. 320-328.
12. Wang, L. B., Tao, W. Q., Wang, Q. W. & Wong, T. T. (2001). Experimental study of developing turbulent flow and heat transfer in ribbed convergent/divergent square ducts. *I. J. of Heat and Fluid Flow*, pp. 603-613.
13. Tanda, G. (2004). Heat transfer in rectangular channels with transverse and V-shaped broken ribs. *I. J. Heat and Mass Transfer*, Vol. 47, pp. 229-243.
14. Scwall, E. A., Tafti, D. K., Graham, A. B. & Thole, K. A. (2006). Experimental validation of large eddy simulations of flow and heat transfer in a stationary ribbed duct. *I. J. of Heat and Fluid Flow*, Vol. 27, pp. 243-258.
15. Patankar, S. V. (1980). *Numerical heat transfer and fluid flow*. Hemisphere, Washington, D. C.
16. Wilcox, D. C. (1988). Reassessment of the scale-determining equation for advanced turbulence models. *AIAA Journal*, Vol. 26, pp. 1299-1310.

17. Abid, R., Rumsey, C. & Gatski, T. (1995). Prediction of non equilibrium turbulent flows with explicit algebraic stress models. *AIAA Journal*, Vol. 33, pp. 2026-2031.
18. Wilcox, D. C. (1993). Comparison of two-equation turbulence models for boundary layers with pressure gradient. *AIAA Journal*, Vol. 31, pp. 1414-1421.
19. Peng, S. H., Davidson, L. & Holmberg, S. (1997). A modified low-Reynolds number $k-w$ model for re-circulating flows. *J. Fluid Engineering*, Vol. 119, pp. 867-875.
20. Iacovides, H., Jackson, D. C., Ji, H., Kelemenis, G. & Launder, B. E. (1996). LDA study of flow development through an orthogonally rotating U-bend of strong curvature and rib-roughened walls. Paper no. ASME-96-GT-476, Int. Gas-Turbine and Aero Congress, Birmingham, UK.
21. Iacovides, H., Jackson, D. C., Ji, H., Kelemenis, G. & Launder, B. E. (1998). LDA study of flow development through an orthogonally rotating U-bend of strong curvature and rib-roughened walls. *J. Turbomachinery*, Vol. 120, pp. 386-391.
22. Myong, H. K. & Kasagi, N. (1990). A new approach to the improvement of k-e turbulence model for wall-bounded shear flows. *JSME Int. J., Ser II*, Vol. 33, No. 1, 63-72.
23. Pope, S. B. (2000). *Turbulence flows*. Cambridge Univ. Press, Cambridge, England.
24. Kays, W. & Crawford, M. (1993). *Convective heat and mass transfer*. McGraw-Hill Inc, New York.